Pattern Formation of Three-Dimensional Electroconvection on a Charge Selective Surface

Soohyeon Kang[1] and Rhokyun Kwak[1,2,*]

[1]Department of Mechanical Engineering, Hanyang University, Seoul 04763, Republic of Korea
[2]Institute of Nano Science and Technology, Hanyang University, Seoul 04763, Republic of Korea

(Received 18 July 2019; revised manuscript received 4 November 2019; accepted 16 March 2020; published 13 April 2020)

When a charge selective surface consumes or transports only cations or anions in the electrolyte, biased ion rejection initiates hydrodynamic instability, resulting in vortical fluid motions called electroconvection. In this Letter, we describe the first laboratory observation of three-dimensional electroconvection on a charge selective surface. Combining experiment and scaling analysis, we successfully categorized three distinct patterns of 3D electroconvection according to $[(\mathrm{Ra}_E)/(\mathrm{Re}^2\mathrm{Sc})]$ [electric Rayleigh number (Ra_E), Reynolds number (Re), Schmidt number (Sc)] as (i) polygonal, (ii) transverse, or (iii) longitudinal rolls. If Re increases or Ra_E decreases, pure longitudinal rolls are presented. On the other hand, transverse rolls are formed between longitudinal rolls, and two rolls are transformed as polygonal one at higher Ra_E or lower Re. In this pattern selection scenario, Sc determines the critical electric Rayleigh number (Ra_E^*) for the onset of each roll, resulting in $\mathrm{Ra}_E^* \sim \mathrm{Re}^2\mathrm{Sc}$. We also verify that convective ion flux by electroconvection (represented by an electric Nusselt number Nu_E) is fitted to a power law, $\mathrm{Nu}_E \sim [(\mathrm{Ra}_E - \mathrm{Ra}_E^*)/(\mathrm{Re}^2\mathrm{Sc})]^{\alpha_1}\mathrm{Re}^{\alpha_2}\mathrm{Pe}^{\alpha_3}$ [Péclet number (Pe)], where each term represents the characteristics of electroconvection, shear flow, and ion transport.

DOI: 10.1103/PhysRevLett.124.154502

Fluid flows are sometimes stable, but often unstable as they fail to sustain flows against small perturbations. This hydrodynamic instability is a classical problem in fluid dynamics, which is relevant to stability theory, pattern formation, and spatiotemporal chaos [1–3]. Recently, a new example of hydrodynamic instability was uncovered in electrochemical systems with a charge selective surface, i.e., electroconvection (EC) [4–6]. Under an electric field, biased cation or anion flux or reaction on a charge selective surface drives the depletion or enrichment of ions on the surface. An ion depletion zone is generated as co-ions are moved out through the surface and counterions are depleted to satisfy electroneutrality in an electrolyte. On the other hand, if co-ions are moved in on the surface, counterions are then accumulated, resulting in an ion enrichment zone. In the so-called ion concentration polarization (ICP), electroconvective instability could arise at the voltage beyond a certain threshold value. So far, three possible mechanisms for this instability have been considered: (i) the electric body force acting on a quasielectroneutral bulk solution (bulk electroconvection) [7,8], (ii) the electric body force acting on an equilibrium electric double layer (electroosmosis of the first kind, a.k.a. equilibrium EC) [9], (iii) the electric body force acting on a nonequilibrium extended space charge layer (electroosmosis of the second kind, a.k.a. nonequilibrium EC) [10,11]. While the driving mechanism for EC is still unresolved, it was found that EC is the main mechanism of the overlimiting current, which can enhance ion flux in various electrochemical systems [6].

With its scientific importance and practical relevance to electrochemical systems, EC has been extensively studied for a decade. However, the research has been primarily concerned with either the first instability that occurs as increasing voltage [4,5] or with the chaotic flow at very high voltage [12,13]. While understanding of spatial pattern formation is crucial for understanding the nonequilibrium fluid system [14], the pattern formation of EC has until recently been beyond the reach of both theory and experiment. Perhaps scientific difficulty regarding EC pattern is due to the general lack of direct observations in three dimensions.

Most previous studies observed EC motions in one dimension [4,5] or two dimensions [12,13], which are oversimplified systems to diversify EC patterns. Indeed, EC has only symmetric vortex structure in 1D/2D geometry under no shear [4,5,15], or shows unidirectional vortices in 2D shear condition [13]. Recently, Demekhin *et al.* [16] and Druzgalski *et al.* [17] analyzed the steady or chaotic 3D structures of EC, but their works were limited to numerical simulation with no shear condition. Pham *et al.* [18] demonstrated that EC has a helical structure only even in 3D geometry under shear flow. Consequently, they all failed to capture an EC pattern variation.

In this Letter, we describe the first direct observation of a 3D EC pattern variation on a charge selective surface. We demonstrate that the EC pattern is diversified in three dimensions under shear flow, according to the Reynolds number (Re), electric Rayleigh number (Ra_E),

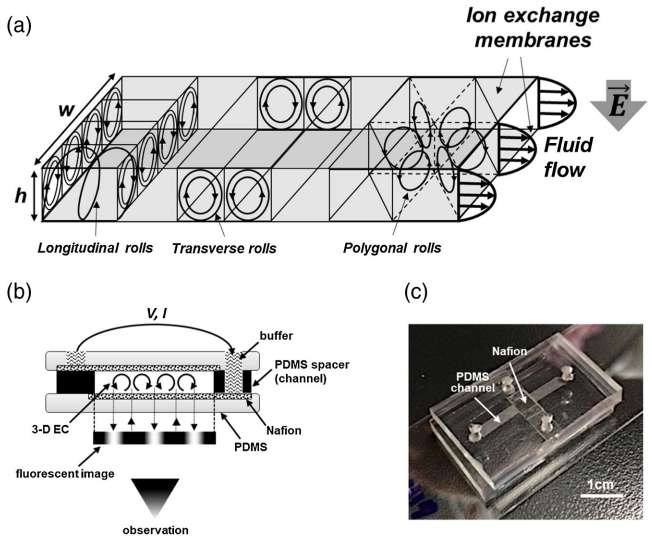

FIG. 1. (a) Schematic diagram of electroconvection in 3D visualization platform between two identical ion-exchange membranes. An electric field $\vec{E}$ is applied vertical to the membranes, and a fluid flow is applied along the membranes. (b) Scheme and (c) picture of the visualization device used in the experiment.

and Schmidt number (Sc) as (i) polygonal, (ii) transverse, or (iii) longitudinal rolls. Scaling analysis with these three nondimensional numbers allows us to pinpoint the threshold for EC pattern variation. Moreover, we verified that the strength of convective ion transport also depends on EC patterns with the shifting of the electric Nusselt number (Nu_E) for the first time.

Our investigation starts with the dimensional analysis of 3D EC to extract parameters that govern its pattern selection. We consider EC between two identical ion-exchange membranes with a channel between them [Fig. 1(a)]. An electrolyte solution flows through this channel. Here are the nondimensional species conservation equation and momentum equation with an electric body force, which governs the EC system (the tilde denotes dimensionless variables, see Supplemental Material for a detailed scaling analysis):

$$\frac{\partial \tilde{c^{\pm}}}{\partial \tilde{t}} + (\tilde{\boldsymbol{U}}\cdot\tilde{\nabla})\tilde{c^{\pm}} = \frac{1}{\mathrm{Pe}}\left[\tilde{D^{\pm}}\tilde{\nabla}\cdot(\tilde{\nabla}\tilde{c^{\pm}}) \pm \frac{F\varphi_0}{RT}\tilde{\nabla}\cdot(\tilde{c^{\pm}}\tilde{\nabla}\tilde{\varphi})\right] \tag{1}$$

$$\frac{\partial \tilde{\boldsymbol{U}}}{\partial \tilde{t}} + (\tilde{\boldsymbol{U}}\cdot\tilde{\nabla})\tilde{\boldsymbol{U}} = -\tilde{\nabla}\tilde{p} + \frac{1}{\mathrm{Re}}\tilde{\nabla}^2\tilde{\boldsymbol{U}} + \frac{\mathrm{Ra}_E}{\mathrm{ReSc}^2}\tilde{\nabla}^2\tilde{\varphi}\tilde{\nabla}\tilde{\varphi} \tag{2}$$

$$\left(\mathrm{Pe} = \frac{U_0 h}{D_{\mathrm{eff}}}, \mathrm{Re} = \frac{U_0 h}{\nu}, \mathrm{Ra}_E = \frac{\varepsilon\varphi_0^2}{\rho\nu D_{\mathrm{eff}}}, \mathrm{Sc} = \frac{\nu}{D_{\mathrm{eff}}}\right), \tag{3}$$

where c^+ and c^- are the concentrations of cations and anions, $\boldsymbol{U}$ is the velocity vector, D^+ and D^- are the diffusivities of cations and anions, F is Faradays constant, R is the gas constant, T is the temperature, φ is the electrical potential, ρ is the density, p is the pressure, ν is the kinematic viscosity, ε is the permittivity, $D_{\mathrm{eff}}[=(2D^+D^-)/(D^+ + D^-)]$ is the effective ion diffusivity, U_0 is the mean velocity, and φ_0 is the applied voltage across the membranes.

In the nondimensional Nernst-Planck equations [Eq. (1)], Péclet number (Pe) denotes ion advection along with the fluid flow against vertical ion diffusion, and this parameter characterizes the shape of concentration boundary layers [19]. In the nondimensional Navier-Stokes equations [Eq. (2)], there are two dimensionless parameters, Re and $[(\mathrm{Ra}_E)/(\mathrm{Re}^2\mathrm{Sc})]$. As we addressed in Kwak *et al.* [13], the pressure $(-\tilde{\nabla}\tilde{p})$ and electric body force $([(\mathrm{Ra}_E)/(\mathrm{Re}^2\mathrm{Sc})]\tilde{\nabla}^2\tilde{\varphi}\tilde{\nabla}\tilde{\varphi})$ terms are balanced with viscous diffusion $[(1/\mathrm{Re})\tilde{\nabla}^2\tilde{\boldsymbol{U}}]$, resulting in pressure-driven flow and EC, respectively. Interestingly, the nondimensional momentum equation and extracted parameters of EC are analogous to that of Rayleigh Bénard convection (RBC) under shear flow [20]. Undeniably, there are clear physical gaps between the two systems. (a) EC often occurs at low Reynolds number, while RBC often occurs at high Reynolds number; generally, there is a size difference of 3–4 orders of magnitude between EC and RBC. (b) EC is initiated by the electric body force near the membrane, while RBC is initiated by the gravitational force acting on the bulk. (c) The electric field in EC (and corresponding electric body force) varies spatiotemporally, while the gravitational field in RBC is constant. However, by comparing the momentum equations of EC and RBC, we can expect that the pattern selections of two systems show similar characteristics. For Poiseuille-RBC, the hydrodynamic instability is generated by the buoyant force, represented as $(\mathrm{Ra}/\mathrm{Re}^2\,\mathrm{Pr})\tilde{T}$ in the dimensionless momentum equation, where Ra is Rayleigh number, Pr is Prandtl number, and $\tilde{T}$ is a dimensionless thermal gradient. Compared with the electric body force term in Eq. (2), $(\mathrm{Ra}_E/\mathrm{Re}^2\mathrm{Sc})\tilde{\nabla}^2\tilde{\varphi}\tilde{\nabla}\tilde{\varphi}$ vs $(\mathrm{Ra}/\mathrm{Re}^2\,\mathrm{Pr})\tilde{T}$, the two source terms of the instability are exactly matched by replacing Ra and Pr to Ra_E and Sc. Physically, we consider ion diffusion (i.e., Sc) instead of thermal diffusion (i.e., Pr) against momentum diffusion, and consider electric body force (i.e., Ra_E) instead of buoyant force (i.e., Ra) against fluid viscosity to generate vortices. In Poiseuille-RBC, previous works confirmed various pattern formation—longitudinal, transverse, or hexagonal rolls—according to Re, Ra, and Pr experimentally and theoretically [20–22]. With reference to these results, we are able to expect that three dimensionless parameters (Re, Ra_E, Sc) will determine the pattern selection of 3D EC in a similar way.

To investigate the 3D motion of EC, we developed a visualization platform using microfluidic tools [Figs. 1(b)–1(c)]. The platform comprises polydimethylsiloxane (PDMS) blocks and a PDMS spacer. On the PDMS blocks, Nafion membranes (Sigma Aldrich Co., Inc., USA), a type

of cation exchange membranes (CEM), were attached to each block. The microchannel was then formed in a thin PDMS spacer by cutting a rectangular channel in it. The width of the channel w is 2 mm, and the height h is 203 μm. The PDMS spacer and the upper PDMS block were bonded first by oxygen plasma treatment. Four holes were then punched on the upper PDMS block: (i) the inlet and outlet of the channel to apply a fluid flow, and (ii) two holes as reservoirs to apply the electric field. Next, the upper PDMS block with spacer and the bottom block were bonded together (see Supplemental Material [23] for a detailed fabrication process).

With this visualization platform, to generate EC under various Sc (556-56127), Ra_E (0-69717), and Re (0-0.447), we controlled the fluid property (i.e., weight percentage of glycerol), applied voltage (0–20 V), and flow rates (0–96 μl/ min), respectively. In order to control Sc, the channel between the membranes was filled with 1 mM sodium chloride glycerol solutions with different glycerol centration (0, 20, 45, 70 wt %, see Supplemental Material [23] for detailed properties). A fluorescent dye (0.83 μM Alexa Flour 633, Invitrogen, CA) was also added into the solutions. This fluorescent dye can visualize EC patterns as the influx of vortex suppresses the depletion zone, visualized as a bright region [Fig. 1(b)]. The bright point can be considered as a current hotspot where the ion flux through the membrane is focused [17]. On the contrary, the outflux of vortex expands the depletion zone, visualized as a dark region. In the reservoir, a high ionic solution (1M NaCl solution without glycerol) was used to compensate for the ICP phenomenon in there. The voltage was applied across the two CEMs using Ag/AgCl electrodes, and the current response was measured with a source-measurement unit (Keithley 2461, Keithley Instruments, Inc., Cleveland, OH). Through the channel, the fluid flow was applied by a syringe pump (Fusion 200, Chemyx, Inc., TX).

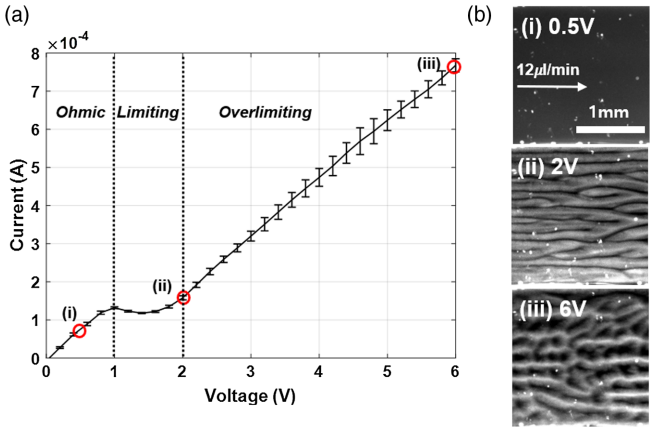

FIG. 2. (a) Current-voltage curve of 45 wt % glycerol solution at 12 μl/ min flow rate. Voltage was ramped up at 0.2 V/2 sec, and current was measured three times repeatedly. (b) Fluorescent images at the voltage of 0.5, 2, and 6 V.

Figure 2 shows a representative current-voltage (I-V) response and visualized EC patterns. In accordance with previous works, the I-V curve can be distinguished in the following three regimes: Ohmic, limiting, and overlimiting [Fig. 2(a)]. First, in the Ohmic regime ($V < 1$ V), a linear ion concentration polarization begins with the application of the voltage. At low voltage, the current linearly increases as voltage increases, indicating a near-constant resistance. At higher voltage, as the ion concentration at the membrane decreases notably, and thus the resistance increases, the slope of the I-V curve decreases gradually. When the ion concentration reaches zero on the membrane, at last, the current is saturated [5,6,12]. This is called the limiting regime ($1\ \mathrm{V} < V < 2\ \mathrm{V}$), and the saturated current is known as a limiting current. In Ohmic-limiting regimes, ions can migrate by electric drift and diffusion only, so we can observe no flow motions except the pressure-driven flow [Fig. 2(b)(i)]. At the voltage over 2 V, EC arises as co-ions are strongly depleted near the membrane [Figs. 2(b)(ii)–(iii)]. In this overlimiting regime, the fluid flow becomes unstable with strong fluctuation of the current, and certain flow patterns by EC begin to appear.

As we expect, the EC pattern can be diversified in our experiment with three distinct shapes as (i) longitudinal, (ii) transverse, or (iii) polygonal rolls (Fig. 3). When the applied voltage is low and/or the flow rate is high, longitudinal rolls with their axes parallel to the flow direction create a horizontal pattern (4 V, 24 μl/ min in Fig. 3). This pattern makes a periodic fluctuation of the fluorescence intensity along an arbitrary vertical line [Supplemental Material [23] Fig. 2(a)], so spatial fast Fourier transform (FFT) of longitudinal rolls show two

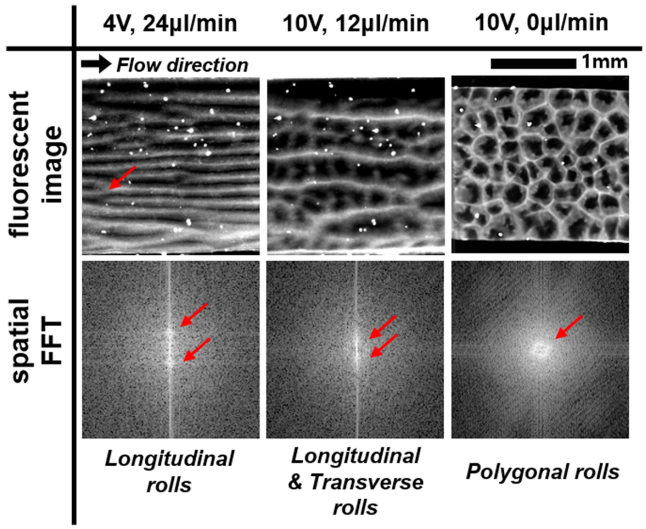

FIG. 3. Fluorescent images of three EC patterns with 0 wt % glycerol solution and their spatial FFT images. A dislocation defect is also observed where the pair of rolls terminates, which exists in RBC and other instabilities too [3]. Videos of three EC patterns are available in the Supplemental Material [23].

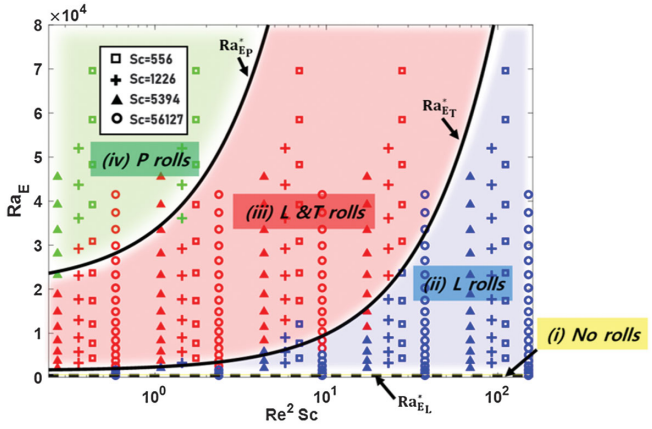

FIG. 4. Phase diagram of 3D EC patterns with respect to Ra_E, Re, and Sc. Four regimes are categorized as (i) no rolls (yellow region), (ii) pure longitudinal rolls (blue region), (iii) longitudinal rolls with transverse rolls (red region), and (iv) polygonal rolls (green region). Logarithmic scale on the x axis is adopted. The full set of fluorescence images are available in Supplemental Material [23].

clear peaks along a vertical line. Next, as the voltage increases and/or the flow rate decreases, transverse rolls with their axes perpendicular to the flow direction occur and create a periodic vertical pattern between horizontal ones [10 V, 12 μl/ min in Fig. 3 and Supplemental Material [23], Fig. 2(b)]. Contrary to the stationary longitudinal rolls, transverse rolls are advected by the mean flow [13,35], so the resultant pattern is not as clear as longitudinal pattern. It is, therefore, hard to identify transverse rolls on the spatial FFT image, which shows a vague circular peak. Meanwhile, in the case of higher voltage and/or lower flow rate, clear polygonal rolls with their omnidirectional axes appear (10 V, 0 μl/ min in Fig. 3). The FFT image of this pattern shows one circular peak in the middle.

Based on the visualization results, four different flow regimes are divided: (i) no rolls, (ii) pure longitudinal rolls, (iii) longitudinal rolls with transverse rolls, and (iv) polygonal rolls (Fig. 4). The boundaries between the regimes can be identified by the critical Ra_E for the onset of EC (with only longitudinal rolls, $\mathrm{Ra}^*_{E_L}$), transverse rolls ($\mathrm{Ra}^*_{E_T}$), and polygonal rolls ($\mathrm{Ra}^*_{E_P}$). First, EC will occur if the electric body force overwhelms the fluid viscosity. Then, the ratio of electric body force to viscosity, $\mathrm{Ra}^*_{E_L}$, has a constant value independent to the other dimensionless numbers. We can see any EC (or not) beyond (or below) $\mathrm{Ra}^*_{E_L} \sim 415$. After EC is initiated, its pattern selection will be determined by the degree of electric body force term, i.e., $[(\mathrm{Ra}_E)/(\mathrm{Re}^2\mathrm{Sc})]\tilde{\nabla}^2\tilde{\varphi}\,\tilde{\nabla}\,\tilde{\varphi}$ in Eq. (2). This also represents the ratio of the electrical energy to the convective energy ($=\varepsilon\varphi_0^2/U_0^2h^2$). The electrical energy is the source to drive the system out of equilibrium, and the convective energy restores the system to a state of equilibrium. Therefore, the same EC pattern has the same value of $[(\mathrm{Ra}_E)/(\mathrm{Re}^2\mathrm{Sc})]$, resulting in

$$\mathrm{Ra}^*_{E_{T,P}} = A\,\mathrm{Re}^2\mathrm{Sc} + B, \tag{4}$$

where A and B are constants. In Fig. 4, the following two equations separate the regimes clearly with high accuracy of 91% [(number of predicted data)/(number of overall data)]: $\mathrm{Ra}^*_{E_T} = 830\,\mathrm{Re}^2\mathrm{Sc} + 1500$, $\mathrm{Ra}^*_{E_P} = 13000\,\mathrm{Re}^2\mathrm{Sc} + 20500$.

It is noted that there is an ongoing debate about the effect of the shear flow on EC. Kwak *et al.* identified three unique characteristics of EC under shear flow (asymmetric EC, vortex advection, size reduction) [35], but Abu-Rjal *et al.* recently addressed that these characteristics can be explained by the superposition of EC in a quiescent fluid and the shear flow [36]. Compared to Abu-Rjal *et al.*, our result also shows that Re does not influence on the initiation of EC. However, pattern formation of EC in this work may not be explained by this simple superposition, because it cannot explain the change of numbers of EC vortices (i.e., EC wavelength). Generally, small seed EC vortices are initially generated on the membrane, and then they are merged together [4,37]. In this situation, we hypothesize that the shear flow governs the favorable direction of vortex merging and determines its final pattern. In three dimensions, seed vortices can merge freely without the shear flow, resulting in an omnidirectional polygonal pattern; whereas seed vortices are hard to merge against the shear flow, resulting in a unidirectional longitudinal pattern. To support our hypothesis, the emergence and evolution of EC are carefully monitored (Supplemental Material [23], Fig. 8 and video 3). At 10 V and 40 μl/ min, right after the voltage is applied ($t < 1$ sec), there are lots of small vortices that form a polygonal pattern. In this initial stage, EC vortices are still small and located only near the membrane (in the low flow velocity region). As these vortices are merging and growing into the higher flow velocity region, they are realigned in longitudinal direction under the shear flow ($t > 1$ sec).

Lastly, we investigate the influence of EC pattern on convective ion flux by calculating an electric Nusselt number, Nu_E (Fig. 5). Nu_E is defined as the ratio of overall ion fluxes (convection + conduction) to the conductive ion flux [35,38,39]. Experimentally, we can present Nu_E by calculating a dimensionless current I/I_{lim}, where the current in overlimiting regime I represents the addition of convective ion flux by EC and the conductive ion flux, and the limiting current I_{lim} represents only conductive ion flux before EC generation. The current response I and limiting current I_{lim} were measured in regimes (ii)–(iv) (Supplemental Material [23], Fig. 9). Here, Nu_E is successfully fitted to a power law,

$$\mathrm{Nu}_E = 0.0018\left(\frac{\mathrm{Ra}_E - \mathrm{Ra}^*_E}{\mathrm{Re}^2\mathrm{Sc}}\right)^{0.48}\mathrm{Re}^{0.09}\mathrm{Pe}^{0.87}, \tag{5}$$

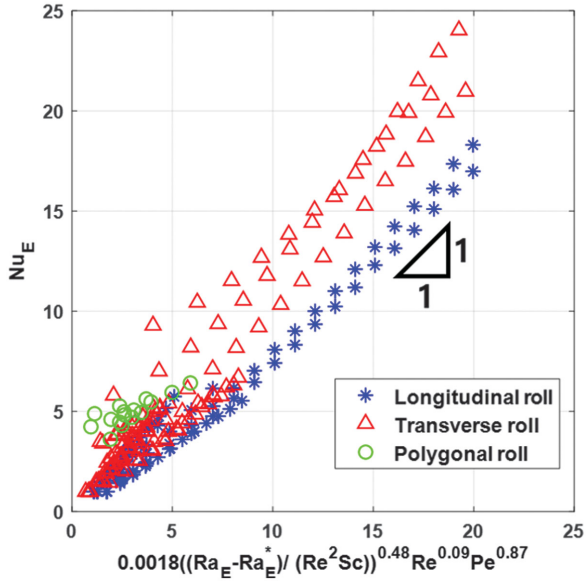

FIG. 5. Nu_E for each roll pattern with a power law $\mathrm{Nu}_E = 0.0018[(\mathrm{Ra}_E - \mathrm{Ra}_E^*)/(\mathrm{Re}^2\mathrm{Sc})]^{0.48}\mathrm{Re}^{0.09}\mathrm{Pe}^{0.87}$.

where Ra_E^* is $\mathrm{Ra}_{E_L}^*$ for regime (ii), $\mathrm{Ra}_{E_T}^*$ for regime (iii), and $\mathrm{Ra}_{E_P}^*$ for regime (iv). We used different Ra_E^* for the different regimes in order to analyze the influence of each roll on Nu_E.

As seen in the Eq. (5), the effect of Re on Nu_E is trivial, compared to that of $[(\mathrm{Ra}_E - \mathrm{Ra}_E^*)/(\mathrm{Re}^2\mathrm{Sc})]$ and Pe. Whereas $[(\mathrm{Ra}_E - \mathrm{Ra}_E^*)/(\mathrm{Re}^2\mathrm{Sc})]$ determines the speed of EC and Pe determines vertical ion diffusion against the shear flow, Re itself represents only ion advection along with the shear flow, which is independent of the vertical ion flux. Moreover, in Fig. 5, Nu_E is higher in the transverse or polygonal roll regime than in the longitudinal roll regime. This increase is probably due to the different characteristics of each roll. Longitudinal rolls are stable and stationary; on the contrary, transverse or polygonal rolls not only advect along with the fluid flow but also change its structure and corresponding local velocity [35,40,41]. Such spatiotemporal changes of the rolls agitate the depletion zones and enhance ion transfer through the membrane [41].

Our experiments and scaling analysis reveal significant insights regarding the pattern selection of EC in 3D systems. Beyond the recent works [4,5,12,13,16–18], it firmly established that 3D EC pattern can be diversified as polygonal, transverse, or longitudinal rolls. In addition, we reveal that new scaling laws govern the choice of EC patterns and corresponding convective ion flux by EC. This characterization of 3D EC opens up the possibility that convective ion transport on charge selective surfaces can be actively tuned by the pattern selection of electroconvection, with potential applications to engineering better electric desalination, fuel cell, and flow batteries.

This work was supported by the Climate Change Response Technology Development Project (NRF-2017M1A2A2047475) and the Basic Research Project (NRF-2019R1C1C1008262) from the National Research Foundation of Korea.

*Corresponding author.
rhokyun@hanyang.ac.kr

[1] G. Ahlers, S. Grossmann, and D. Lohse, Rev. Mod. Phys. **81**, 503 (2009).
[2] T. T. Al-Housseiny, P. Tsai, and H. A. Stone, Nat. Phys. **8**, 747 (2012).
[3] M. C. Cross and P. C. Hohenberg, Rev. Mod. Phys. **65**, 851 (1993).
[4] I. Rubinstein and B. Zaltzman, Phys. Rev. E **62**, 2238 (2000).
[5] S. M. Rubinstein, G. Manukyan, A. Staicu, I. Rubinstein, B. Zaltzman, R. G. H. Lammertink, F. Mugele, and M. Wessling, Phys. Rev. Lett. **101**, 236101 (2008).
[6] V. V. Nikonenko, A. V. Kovalenko, M. K. Urtenov, N. D. Pismenskaya, J. Han, P. Sistat, and G. Pourcelly, Desalination **342**, 85 (2014).
[7] A. P. Grigin, Electrokhimia **21**, 52 (1985).
[8] I. Rubinstein, E. Staude, and O. Kedem, Desalination **69**, 101 (1988).
[9] I. Rubinstein and B. Zaltzman, Phys. Rev. Lett. **114**, 114502 (2015).
[10] S. Dukhin, Adv. Colloid Interface Sci. **35**, 173 (1991).
[11] I. Rubinstein and L. Shtilman, J. Chem. Soc. Faraday Trans. **75**, 231 (1979).
[12] R. Kwak, G. Guan, W. K. Peng, and J. Han, Desalination **308**, 138 (2013).
[13] R. Kwak, V. S. Pham, K. M. Lim, and J. Han, Phys. Rev. Lett. **110**, 114501 (2013).
[14] M. Cross and H. Greenside, *Pattern Formation and Dynamics in Nonequilibrium Systems* (Cambridge University Press, Cambridge, England, 2009).
[15] J. C. de Valenca, M. Wagterveld, R. Lammertink, and P. Tsai, Phys. Rev. E **92**, 031003 (2015).
[16] E. A. Demekhin, N. V. Nikitin, and V. S. Shelistov, Phys. Rev. E **90**, 013031 (2014).
[17] C. Druzgalski and A. Mani, Phys. Rev. Fluids **1**, 073601 (2016).
[18] S. V. Pham, H. Kwon, B. Kim, J. K. White, G. Lim, and J. Han, Phys. Rev. E **93**, 033114 (2016).
[19] R. Kwak, V. S. Pham, B. Kim, L. Chen, and J. Han, Sci. Rep. **6**, 25349 (2016).
[20] C. Yu, M. Chang, and T. Lin, Int. J. Heat Mass Transfer **40**, 333 (1997).
[21] S. S. Chen and A. S. Lavine, Int. J. Heat Mass Transfer **39**, 1 (1996).
[22] X. Nicolas, J.-M. Luijkx, and J.-K. Platten, Int. J. Heat Mass Transfer **43**, 589 (2000).
[23] See Supplemental Material at http://link.aps.org/supplemental/10.1103/PhysRevLett.124.154502 for further details, which includes Refs. [19,24–34].
[24] N. S. Cheng, Ind. Eng. Chem. Res. **47**, 3285 (2008).
[25] S. Hoshino and K. Sato, Chem. Eng. **31**, 961 (1967).
[26] P. S. Albright, J. Am. Chem. Soc. **59**, 2098 (1937).

[27] H. Tyrrell and K. Harris, *Diffusion in Liquids: A Theoretical and Experimental Study* (Butterworths, London, 1984).
[28] J. T. Su, P. B. Duncan, A. Momaya, A. Jutila, and D. Needham, J. Chem. Phys. **132**, 044506 (2010).
[29] A. E. Marcinkowsky, H. Phillips, and K. A. Kraus, J. Phys. Chem. **72**, 1201 (1968).
[30] G. L. Pollack, R. P. Kennan, J. F. Himm, and P. W. Carr, J. Chem. Phys. **90**, 6569 (1989).
[31] R. Robinson and R. Stokes, *Electrolyte Solutions: Second Revised Edition* (Dover Publications, Mineola, 2002).
[32] B. A. Kowert, R. M. Turner, and C. V. C. Caldwell, Chem. Phys. **344**, 114 (2008).
[33] S. G. Schultz and A. K. Solomon, J. Gen. Phys. **44**, 1189 (1961).
[34] R. Mills and V. Lobo, *Self-Diffusion in Electrolyte Solutions: A Critical Examination of Data Compiled from the Literature* (Elsevier Science, Amsterdam, 2013).
[35] R. Kwak, V. S. Pham, and J. Han, J. Fluid Mech. **813**, 799 (2017).
[36] R. Abu-Rjal, L. Prigozhin, I. Rubinstein, and B. Zaltzman, Russ. J. Electrochem. **53**, 903 (2017).
[37] T. Pundik, I. Rubinstein, and B. Zaltzman, Phys. Rev. E **72**, 061502 (2005).
[38] K. Luo, J. Wu, H.-L. Yi, and H.-P. Tan, Phys. Fluids **30**, 023602 (2018).
[39] J. C. Lacroix, P. Atten, and E. J. Hopfinger, J. Fluid Mech. **69**, 539 (1975).
[40] M. Urtenov, A. Uzdenova, A. Kovalenko, V. Nikonenko, N. Pismenskaya, V. Vasil'eva, P. Sistat, and G. Pourcelly, J. Membr. Sci. **447**, 190 (2013).
[41] V. Nikonenko, V. Vasil'eva, E. Akberova, A. Uzdenova, M. Urtenov, A. Kovalenko, N. Pismenskaya, S. Mareev, and G. Pourcelly, Adv. Colloid Interface Sci. **235**, 233 (2016).